Opto-Electronic Advances

Article

July 2023, Vol. 6, No. 7

DOI: 10.29026/oea.2023.220073

All-optical controlled-NOT logic gate achieving directional asymmetric transmission based on metasurface doublet

Yijia Huang[1†], Tianxiao Xiao[2†], Shuai Chen[4], Zhengwei Xie[1], Jie Zheng[1], Jianqi Zhu[1], Yarong Su[1], Weidong Chen[1], Ke Liu[1], Mingjun Tang[1], Peter Müller-Buschbaum[2,3*] and Ling Li[1*]

Optical logic gates play important roles in all-optical logic circuits, which lie at the heart of the next-generation optical computing technology. However, the intrinsic contradiction between compactness and robustness hinders the development in this field. Here, we propose a simple design principle that can possess multiple-input-output states according to the incident circular polarization and direction based on the metasurface doublet, which enables controlled-NOT logic gates in infrared region. Therefore, the directional asymmetric electromagnetic transmission can be achieved. As a proof of concept, a spin-dependent Janus metasurface is designed and experimentally verified that four distinct images corresponding to four input states can be captured in the far-field. In addition, since the design method is derived from geometric optics, it can be easily applied to other spectra. We believe that the proposed metasurface doublet may empower many potential applications in chiral imaging, chiroptical spectroscopy and optical computing.

Keywords: metasurface; polarization control; asymmetric transmission; logic gate

Huang YJ, Xiao TX, Chen S, Xie ZW, Zheng J et al. All-optical controlled-NOT logic gate achieving directional asymmetric transmission based on metasurface doublet. *Opto-Electron Adv* **6**, 220073 (2023).

Introduction

Since the information processing efficiency for traditional electron-based computing technology with excessive Ohmic loss is intrinsically limited by the RC delay as well as the data transfer speed among different modules, optical computing is a promising alternative[1,2]. Due to its unique properties of ultrahigh processing speed, ultralow power consumption and parallel operation capability for ref.[3,4], optical computing has been treated as a potential platform to meet the demands for large calculation amount and low-cost energy consumption. Akin to its electron-based counterpart, logic operations are also required in optical circuits to lay the foundation for the implementation of computing. Therefore, constructing and exploring all-optical logic gates (LGs) with robust performance, complete logic function and ease of

[1]Laboratory of Micro-Nano Optics, College of Physics and Electronic Engineering, Sichuan Normal University, Chengdu 610101, China; [2]Physik-Department, Lehrstuhl für Funktionelle Materialien, Technische Universität München, James-Franck-Straße 1, 85748, Garching, Germany; [3]Heinz Maier-Leibnitz Zentrum (MLZ), Technische Universität München, Lichtenbergstraße. 1, 85748, Garching, Germany; [4]Tianjin Huahuixin Technology Group Co., Ltd, Zhongtian Avenue, Tianjin 300467, China.

†These authors contributed equally to this work.

*Correspondence: P Müller-Buschbaum, E-mail: muellerb@ph.tum.de; L Li, E-mail: lingli70@aliyun.com

Received: 15 April 2022; Accepted: 13 July 2022; Published online: 18 January 2023

implementation is now a hotspot in the fields of optics, plasmonics and photonics[5].

To date, although many related works have been reported to achieve all-optical logic operations based on linear or nonlinear optical effects, their performances are still limited by their intrinsic drawbacks. For nonlinear cases[6–8], since the optical LGs are mostly based on the third-order nonlinear susceptibility that heavily depends on the precise manipulation of control light and pump light, the robustness for these devices can hardly meet the requirements for practical applications. For linear cases, the methodologies mainly include interference effects and on-chip plasmonic effects[9–12]. The limitation for the former one is the rigid interference conditions and complicated optical paths, which lead to performance instability as well as device cumbersome[11,12], while the latter one is restricted by stringent demand for the size of input beams to avoid cross talk and false output[9,10].

Metasurface, as a kind of artificial surface composed of subwavelength unit cells, has attracted much attention in recent years due to its unique properties such as small footprints, flexible functions and planar geometries[13–17]. By ingeniously aligning the meta atoms and choosing proper materials, many novel phenomena and applications have been witnessed including electromagnetic absorption[18–23], flat lensing[24–28], surface cloaking[29,30], polarization control[31–36] and meta-hologram[37–40]. Recently, metasurface-based all-optical LGs were also proposed that have already manifested many exotic advantages over the traditional counterparts due to their more compact structures and higher operation efficiency[5,41–43]. However, most of the presented works only realized basic LGs with "AND", "OR" or "NOT" operations, while additional logic operations will be needed for practical application.

Here, in order to further enhance the operation robustness and miniature of the optical device, we propose a metasurface-based all-optical LG with simple yet generalized methodology. Distinct from previously reported works that need specific manipulations for the incident light, this designed all-optical LG exhibits a highly efficient response simply under plane wave incidence according to its incident direction and spin state. Besides, it possesses multiple-input-output states that behave as a controlled-NOT (CNOT) LG. Similar to its quantum counterpart[44,45], control signal (CS) ε_1 and target signal (TS) ε_2 are two basic elements in the all-optical CNOT LG. Mathematically, such operation can be described as:

$$|\varepsilon_1\rangle\,|\varepsilon_2\rangle \rightarrow |\varepsilon_1\rangle\,|\varepsilon_1 \oplus \varepsilon_2\rangle\ , \tag{1}$$

where $\varepsilon_{1,2}$=0 or 1 describes their incident states and $\oplus$ denotes the logic modulation. As shown in Eq. (1), the input CS determines the change of TS and the value of CS is invariant during the operation. Therefore, the CNOT LG can be expressed by the unitary operation:

$$\begin{array}{c} \\ |00\rangle \\ |01\rangle \\ |10\rangle \\ |11\rangle \end{array} \begin{array}{c} \begin{array}{cccc} |00\rangle & |01\rangle & |10\rangle & |11\rangle \end{array} \\ \begin{pmatrix} 1 & 0 & 0 & 0 \\ 0 & 1 & 0 & 0 \\ 0 & 0 & 0 & 1 \\ 0 & 0 & 1 & 0 \end{pmatrix} \end{array} . \tag{2}$$

Equation (2) shows that if the input CS equals "0", the output TS maintains its value. Otherwise, the output TS will be altered accordingly ("0" to "1" or "1" to "0"). To further present the working mechanism of the proposed metasurface-based CNOT LG, Fig. 1 shows the far-field responses after incident light passing through the metasurface doublet under different conditions. It can be inferred that four diverse responses can be obtained, which perfectly match with the demand for aforementioned CNOT LG. In this case, CS is the spin state of incident light, while its incident direction is TS.

Design and methods

To illustrate the mechanism for the aforementioned all-optical CNOT LG, we begin with the analysis of a typical anisotropic unit cell as shown in Fig. 2(a). According to the theory of geometric phase (also known as Pancharatnam-Berry phase)[46], when plane wave $\boldsymbol{E}$ impinges on such transparent optical scatterer, the transmission electromagnetic field $\boldsymbol{E}'$ can be linked with $\boldsymbol{E}$ by a Jones matrix as

$$\boldsymbol{E}' = \begin{pmatrix} \cos\dfrac{\delta}{2} & \mathrm{i}\sin\dfrac{\delta}{2}\mathrm{e}^{-2\mathrm{i}\varphi} \\ \mathrm{i}\sin\dfrac{\delta}{2}\mathrm{e}^{2\mathrm{i}\varphi} & \cos\dfrac{\delta}{2} \end{pmatrix} \boldsymbol{E}\ , \tag{3}$$

where δ is the phase difference between orthogonal linear polarizations, φ is the orientation angle between the unit cell main axis and x axis. Therefore, Eq. (3) can be further simplified as

$$\begin{aligned} \boldsymbol{E}' = \cos\left(\frac{\delta}{2}\right)\boldsymbol{E} - \mathrm{i}\sin\left(\frac{\delta}{2}\right) \times [\langle \boldsymbol{E} \mid R\rangle \exp(-\mathrm{i}2\varphi)\,|L\rangle \\ + \langle \boldsymbol{E} \mid L\rangle \exp(\mathrm{i}2\varphi)\,|R\rangle], \end{aligned} \tag{4}$$

where $|L\rangle$ and $|R\rangle$ denote left- (LCP) and right-handed circularly polarized (RCP) waves, respectively. The first term in the right side of Eq. (4) indicates that a part of the output beam keeps the same polarization as the

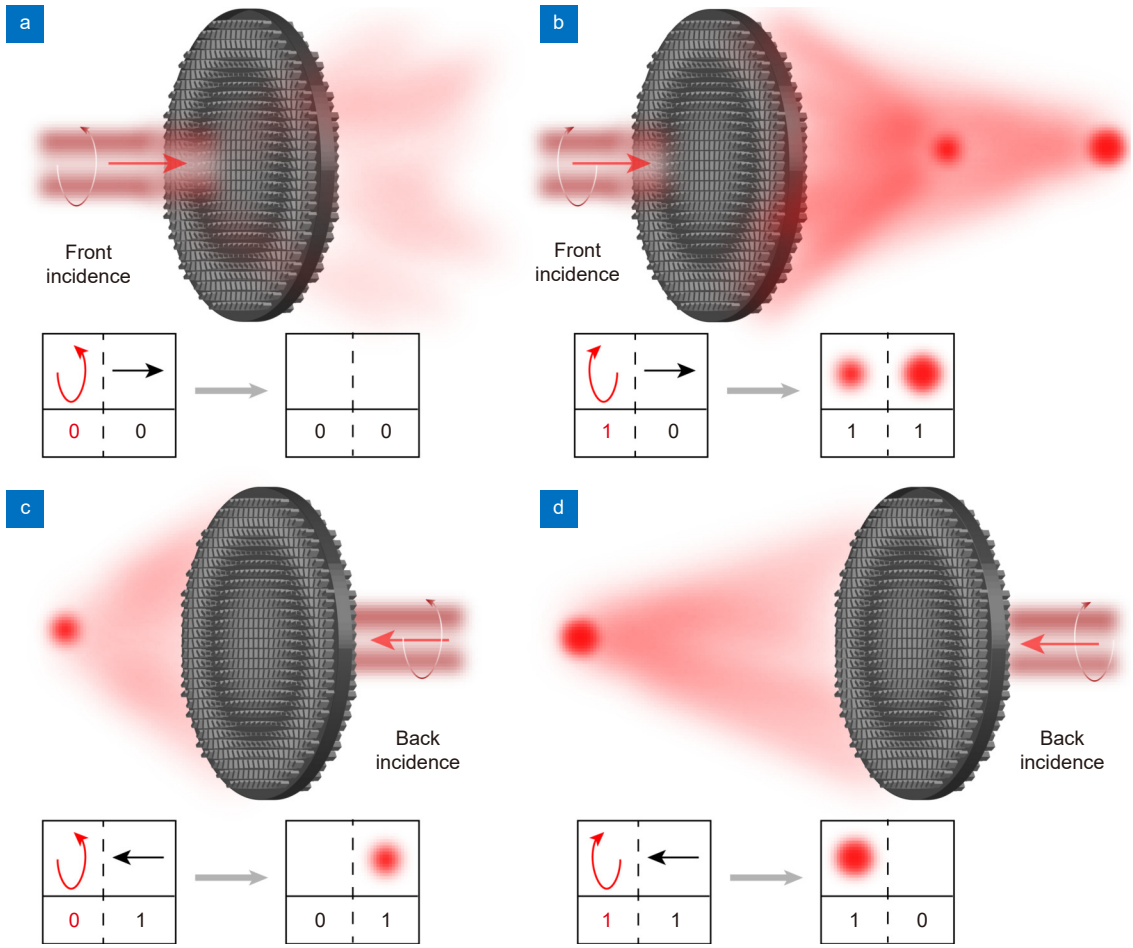

Fig. 1 | Schematic for the proposed all-optical CNOT LG. (**a**–**d**) Far-field responses under different incident conditions that correspond to (a) no focus, (b) two foci, (**c**) one focus with small focal distance and (d) one focus with large focal distance. The corresponding truth-table is shown in the inset with spin state as CS and incident direction as TS, which is perfectly matched with that in Eq. (2).

incidence without phase shift, while the second term shows that another part of the output beam will reverse its spin and acquire an extra phase shift depending on φ, which is defined as geometric phase. Thus, in order to increase the operation efficiency, the ideal unit cell for most of the geometric phase based metasurfaces is a high-performance half wave plate (HHWP) with $\delta=\pi$ and the co-polarized transmitted waves are generally treated as noises. Since incident light with opposite spins will experience reversed phase shifts, these metasurfaces exhibit conjugated directional performance as shown in Fig. S1. It should be mentioned that although recent design methods can decouple the spin-dependent phase response by combining geometric phase with propagation phase[47,48], the conjugated responses are still existing so that the phase shift under LCP front incidence (RCP front incidence) is always equal to that under RCP back incidence (LCP back incidence).

To break the spin-dependent directional transmission conjugation, we propose a metasurface doublet with a metasurface (M1) composed of HHWP unit cells at the front side and another metasurface (M2) composed of low-performance half wave plate (LHWP) unit cells with $\delta=\pi/2$ at the back side. In the simulation, the device is all-silicon with permittivity obtained from measurement[49] and the details are given in the Experimental section. It can be inferred from Fig. 2(b) and 2(f) that the polarization conversion ratio (defined as the transmittance of cross-polarized light to transmitted light) at 28.3 THz is larger than 98% for HHWP unit cell and about 50% for LHWP unit cell. Besides, the simulated phase delays in Fig. 2(b) and 2(f) are well accorded with the geometric phase that the implemented phase θ of the unit cells is solely dependent on their orientation angle φ with $\theta=\pm2\varphi$, where $\pm$ is determined by the incident spin. Therefore, the transmitted light can be fully manipulated by the HHWP unit cells, while only half of the transmitted light is manipulated by the LHWP unit

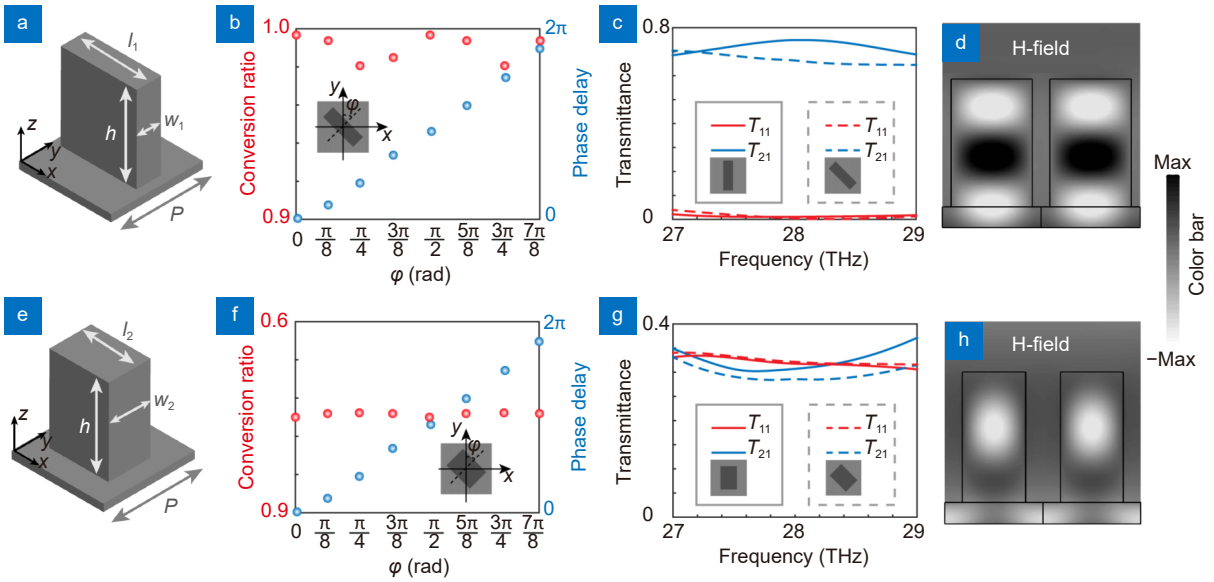

Fig. 2 | Unit cells for the CNOT LG metasurface doublet. (**a**) and (**e**) Schematic for HHWP and LHWP unit cells, respectively. P=4.5 μm, h=6 μm, l_1=3.7 μm, w_1=1.2 μm, l_2=2.9 μm and w_2=2.05 μm. (**b**) and (**f**) Corresponding polarization conversion ratio (left panel) and phase delay (right panel) with different φ for cross-polarized waves at 28.3 THz under LCP incidence. (**c**) and (**g**) Corresponding transmittance at φ=0 (solid lines) and φ=π/4 (dashed lines) from 27–29 THz. (**d**) and (**h**) Corresponding magnetic field distributions at –28.3 THz.

cells. Figure S2 performs a full-wave simulation for beam deflection to further illustrate this issue. Furthermore, the results in Fig. 2(c) and 2(h) indicate that the transmittance of proposed unit cells is nearly unchanged with different orientation angles. The physical mechanism for the HHWP and LHWP can be attributed to different magnetic couplings in the two cases as shown in Fig. 2(d) and 2(g). Apparently, the magnetic field enhancement in the former case is much larger than that in the latter one, which explains the difference for polarization conversion.

Results and discussions

In order to achieve highly efficient all-optical CNOT LG, M1 is designed as a convex lens for LCP front (RCP back) incidence with focal distance f_1, and M2 is also designed as a convex lens for LCP front (RCP back) incidence with focal distance f_2. Therefore, due to the transmission conjugation of the geometric phase, both metalenses are concave lenses for RCP front incidence and LCP back incidence with focal distances $-f_1$ and $-f_2$, respectively. In this case, the transmitted field under certain incident direction and spin state can be calculated simply by geometric optics[50]. Figure S3 gives detailed deductions for the calculation when the substrate thickness d is assumed to be much smaller than f_1 and f_2. It should be mentioned that in all four cases the output can be divided to two parallel parts: One is solely given by M1 with a focal distance $\pm f_1$, the other is the doublet effect by M1 and M2 that the focal distance f_3 can be calculated as $f_3=\pm|(f_1f_2)/(f_1-f_2)|$, where ± is determined by the incident spin and direction. Apparently, a positive focal distance indicates that the focal spot can be observed in the transmitted side, otherwise the focal spot cannot be observed.

To further illustrate this issue, Fig. 3 depicts corresponding numerical results based on vectorial diffraction theory[51]. In this case, the phase delay and the transmitted amplitude of the metasurface doublet are retrieved from the simulated results for the unit cells. The diameter of the metasurface doublet is d_1=6 mm, the focal distances f_1 and f_2 are set as $3d_1$ and $9d_2$. It can be inferred that focal spots can be observed at two locations at z=18 mm (f_1, white dashed lines) and 27 mm (f_3, blue dashed lines), which matches well with the results calculated by geometric optics. The calculated intensity contrast ratio (ICR) is defined as $ICR=I_1/I_0$, where I_1 and I_0 indicate the intensity at a certain position, and the subscripts (1 or 0) are according with those in the insets of Fig. 3. The calculated ICRs are larger than 30.2 dB at $z=f_1$ and 26.8 dB at $z=f_3$ which demonstrates the robustness of the proposed method. In fact, the ICR can be further increased simply by enlarging the size of device or shortening the focal distance. Full-wave simulations are performed using the time domain solver of the commercial software CST Microwave Studio and the corresponding results are

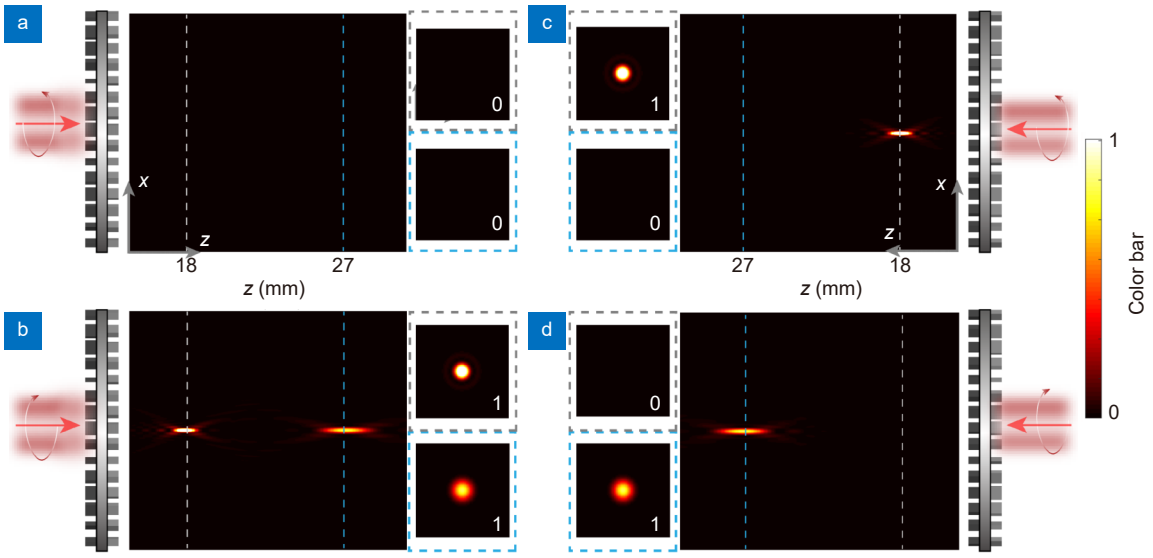

Fig. 3 | Numerical far-field results in *x*-*z* plane under different incident conditions. (**a**) Front RCP incidence. (**b**) Front LCP incidence. (**c**) Back RCP incidence. (**d**) Back LCP incidence. The insets show the 2D normalized intensity distributions at *z*=18 mm (white dashed lines) and 27 mm (blue dashed lines). When a focal spot can be observed at certain focal plane, the corresponding truth table is "1", otherwise the truth table is "0".

shown in Fig. S3. It can be inferred that the simulated results match well with their calculated counterparts that four different outputs can be clearly observed.

As a proof of concept, corresponding experiments are carried out as shown in Fig. 4. Figure 4(a) depicts SEM images of the fabricated M1 and M2 with negligible surface roughness and vertical sidewalls with a sidewall angle >80° (details of the fabrication process is given in the Experimental section). The schematic illustration of the measurement setup is shown in Fig. 4(b) and the optical path in experiment is shown in Fig. S4. A CO_2 laser with working frequency of 28.3 THz is used as the light source. After passing through an attenuator to adjust the intensity, the incident wave will propagate through a linear polarizer (LP) followed by a quarter-wave plate ($\lambda/4$). Then the generated circularly polarized beam will pass through a beam expander (BE) and illuminate on the sample (SA). An infrared charge-coupled device (CCD) (640 × 512 pixels, pixel size 12 μm × 12 μm) is used to measure the far-field images. By changing the angle between the main axes of LP and $\lambda/4$, the spin state of the generated circularly polarized wave can be altered. The measured results are given in Fig. 4(c–f) that correspond to their theoretical counterparts in the insets of Fig. 3(a–d), respectively. The cross section views on the focal plane for the four cases are shown in Fig. S5 with measured ICRs of 8.6 dB at $z=f_1$ and 8 dB at $z=f_3$. The measured results are smaller than the calculated results, which may be due to two reasons. Firstly, the background noise for the infrared CCD cannot be eliminated that will decrease the obtained ICR. Secondly, the imperfect fabrication of the metasurface will also unavoidably influence the performance of the device. Besides, due to the wavelength-independent nature of the geometric phase of the unit cells as shown in Fig. 2(c) and 2(g), the proposed all-optical CNOT LG can work efficiently within a certain bandwidth. For instance, Fig. S6 depicts corresponding results at 27 and 29 THz, demonstrating that a similar performance can be realized as that in Fig. 3 except for the slight shift of the focal distance. To demonstrate the advantages of the proposed all-optical CNOT LG, a comparison between the proposed device and other previously reported works is shown in Table S1 in the Supplementary information.

In fact, except for the above mentioned case, the focal spot can also be shaped by adding extra phase shifts. For example, Fig. S7 shows the results when a vortex phase is added to M2. In this case, a donut-shaped focal spot can be observed at $z=f_3$. Moreover, a promising application for the all-optical CNOT LG is to achieve asymmetric electromagnetic transmission for information encryption. Although previously reported Janus metasurfaces were able to realize directional asymmetric transmission, the method is designed for single polarization that half of the incident power is intrinsically blocked due to supercell strategy[52,53]. Since the proposed metasurface doublet can achieve multiple-input-output performance, it can be used to design Janus metasurfaces for both orthogonal polarizations as shown in Fig. 5. Figure 5(a) shows the

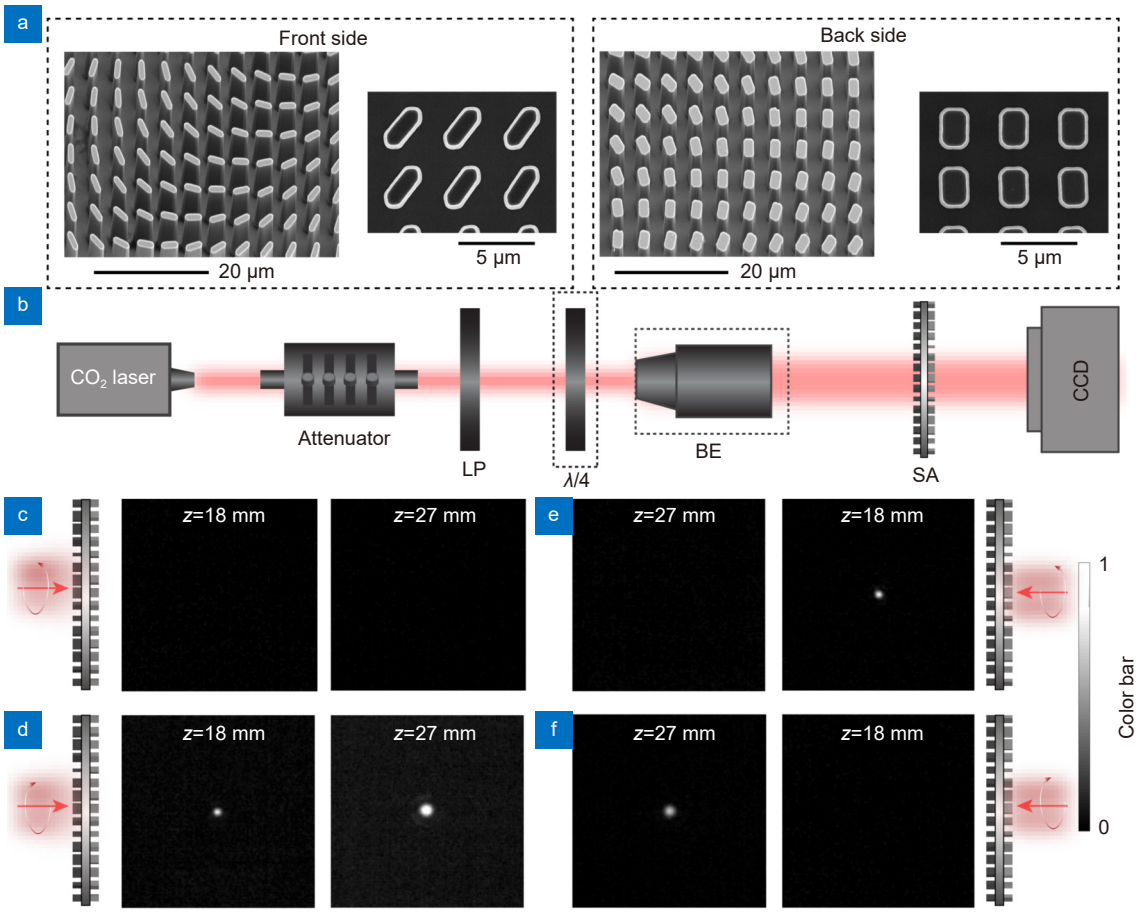

Fig. 4 | Experiment for the asymmetric transmission metasurface doublet. (**a**) SEM images for the front (left) and back (right) side of the metasurface. (**b**) Schematic illustration of the measurement setup. LP: linear polarizer. *λ*/4: quarter wave plate. BE: beam expander. SA: sample. (**c**)-(**f**) Intensity distributions at *z*=18 mm and 27 mm. (c) Front RCP incidence. (d) Front LCP incidence. (e) Back RCP incidence. (f) Back LCP incidence.

schematic flow chart of the design process which is similar to that in ref.[54]. Firstly, the phase distributions φ_1 and φ_2 for the two original images "32" and "35" are obtained by point source algorithm, respectively. Then, the orientations of HHWP unit cells on the front side of the Janus metasurface are determined by geometric phase according to φ_1. Since the image plane of the designed Janus metasurface with the size of 1 mm^2 is designed at 30 mm away from the front side, considering the thickness of the substrate of 0.5 mm, φ_2 is designed so that the distance from the image plane to the back of the metasurface is 29.5 mm. Secondly, the phase distribution φ_3 for "32" on the back side of the Janus metasurface is obtained from φ_1 by considering the propagation phase in the substrate with fast Fourier transformation (FFT) and inverse fast Fourier transformation (IFFT). Lastly, the orientation of the LHWP unit cells on the back side of the Janus metasurface is obtained by combining φ_2 and φ_3. The calculated and measured far-field images at the image plane at different conditions are given in Fig. 5(b–e). The measured optical path is the same as that in Fig. 4(b). Due to limited size of the CCD, only part of the images can be captured in the experiment. It can be inferred from Fig. 5(d) and 5(e) that the target images "32" and "35" can be obtained under RCP and LCP back incidence, respectively. When the incident direction is opposite, the far-field images under LCP and RCP incidence are changed to "38" and none as shown in Fig. 4(b) and 4(c), respectively. It should be mentioned that the distance from the designed image plane to the metasurface for the four cases in Fig. 5 is the same and the target images can still be well observed with low cross talk. Therefore, different information can be encoded to the Janus metasurface depending on the incident spin and propagation direction. Although the result presented in Fig. 5(b) exhibits no specific image, it is theoretically possible to encode arbitrary information in this channel, which has been demonstrated by other works[55,56].

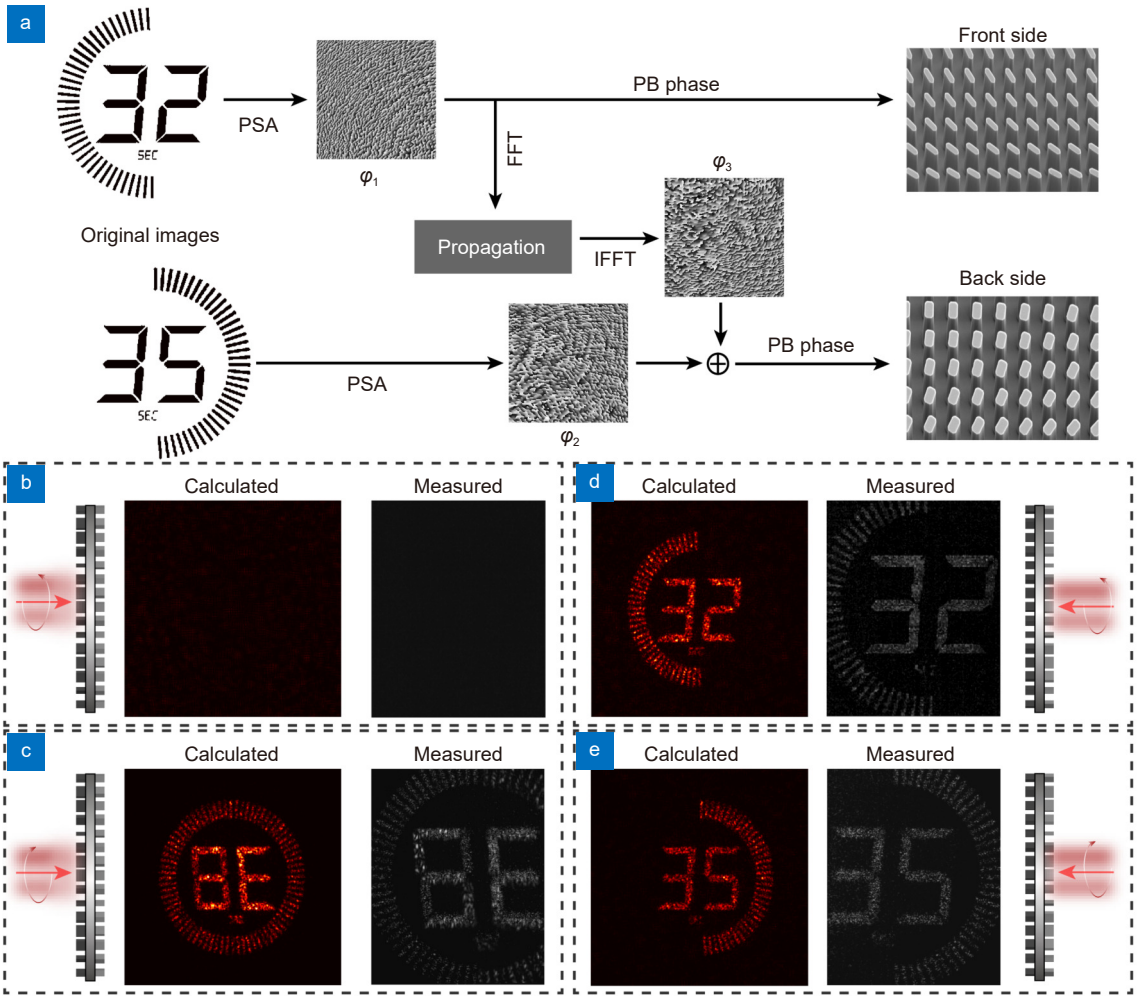

Fig. 5 | Demonstration of the directional Janus metasurface for orthogonal polarizations. (**a**) Schematic flow chart of the design process. FFT: fast Fourier transformation. IFFT: inverse fast Fourier transformation. (**b**)-(**e**) Calculated and measured far-field images at the same image plane under different incident conditions. (b) Front RCP incidence. (c) Front LCP incidence. (d) Back RCP incidence. (e) Back LCP incidence.

Conclusion

In fact, from the perspective of geometric optics, the proposed device in Fig. 3 can also be treated as a spin-selective directional metalens. Different from previously reported works with symmetrical and fixed imaging performance[24,25], the proposed metasurface doublet has the capability to adjust the focal distance (as shown in Fig. 3(c) and 3(d)) or achieve dual imaging at two image planes (as shown in Fig. 3(b)), which may find many exciting applications for chiral sensing and imaging[57–59]. Besides, since the polarization conversion ratios for the fabricated HHWP and LHWP unit cells may differ from the simulated results due to the imperfection of fabrication, we also discuss the influence of such deviation on the performance of the proposed devices in the Supplementary information.

In summary, we propose a simple yet powerful design methodology to achieve an all-optical CNOT LG with metasurface doublet. By ingeniously aligning two metasurfaces with different polarization conversion ratios and phase distributions, multiple input-output performance can be realized depending on the incident spin state and direction. Both theoretical and measured results demonstrate the robustness and broadband nature of the designed device. Furthermore, a CNOT LG-based Janus metasurface is also characterized and shows that the asymmetric electromagnetic transmission can be achieved for orthogonal circularly polarized incidence. Since the design method is derived from geometric optics, it can be easily extended to other part of the spectrum, which will enable more fascinating applications in optical computing, chiral optics and electromagnetic communications.

Experimental section

Numerical simulation: Considering the symmetry of the

structure, to reduce the amount of calculation, the simulated results in Fig. 2 were obtained using the finite element method in CST Microwave Studio with unit cell boundaries in *xy* directions and open boundary in *z* direction. A fine tetrahedral mesh was applied with adaptive mesh refinement to ensure the accuracy of the results. The magnetic field distributions were calculated by using the build-in magnetic field monitors in CST Microwave Studio.

Device fabrication: The schematic diagram of the fabrication process is shown in Fig. S8. The proposed devices were mainly fabricated by ultraviolet lithography and inductively coupled plasma (ICP) etching processes. Firstly, a 1 μm thick SiO_2 layer was coated on the back side of the cleaned double-polished silicon substrate as the protect layer by plasma enhanced chemical vapor deposition (PECVD). Then, a 1 μm thick positive photoresist (AZ5214) was spin-coated onto the front side of the substrate and prebaked at 110 °C for 1 min, followed by the ultraviolet lithography and corresponding developing processes. Next, ICP etching was used to fabricate the HHWP unit cells on the front side, and the photoresist was removed after etching. Then, a 6 μm thick SiO_2 layer was coated on the front side of the substrate to protect the fabricated unit cells. After etching the protect SiO_2 layer on the back side, the same processes were carried out to fabricate the LHWP unit cells on the back side. Lastly, the protect SiO_2 layer on the front side was etched. The tested alignment accuracy between the doublet was within 1.5 μm.

References

1. Caulfield HJ, Dolev S. Why future supercomputing requires optics. *Nat Photonics* **4**, 261–263 (2010).
2. Kirchain R, Kimerling L. A roadmap for nanophotonics. *Nat Photonics* **1**, 303–305 (2007).
3. Silva A, Monticone F, Castaldi G, Galdi V, Alù A et al. Performing mathematical operations with metamaterials. *Science* **343**, 160–163 (2014).
4. Zhu TF, Zhou YH, Lou YJ, Ye H, Qiu M et al. Plasmonic computing of spatial differentiation. *Nat Commun* **8**, 15391 (2017).
5. Qian C, Lin X, Lin XB, Xu J, Sun Y et al. Performing optical logic operations by a diffractive neural network. *Light Sci Appl* **9**, 59 (2020).
6. McCutcheon MW, Rieger GW, Young JF, Dalacu D, Poole PJ et al. All-optical conditional logic with a nonlinear photonic crystal nanocavity. *Appl Phys Lett* **95**, 221102 (2009).
7. Tucker RS. The role of optics in computing. *Nat Photonics* **4**, 405 (2010).
8. Xu QF, Lipson M. All-optical logic based on silicon micro-ring resonators. *Opt Express* **15**, 924–929 (2007).
9. Sang YG, Wu XJ, Raja SS, Wang CY, Li HZ et al. Broadband multifunctional plasmonic logic gates. *Adv Opt Mater* **6**, 1701368 (2018).
10. Fu YL, Hu XY, Lu CC, Yue S, Yang H et al. All-optical logic gates based on nanoscale plasmonic slot waveguides. *Nano Lett* **12**, 5784–5790 (2012).
11. Liu Q, Ouyang ZB, Wu CJ, Liu CP, Wang JC. All-optical half adder based on cross structures in two-dimensional photonic crystals. *Opt Express* **16**, 18992–19000 (2008).
12. Zavalin AI, Shamir J, Vikram CS, Caulfield HJ. Achieving stabilization in interferometric logic operations. *Appl Opt* **45**, 360–365 (2006).
13. Luo XG, Pu MB, Guo YH, Li X, Zhang F et al. Catenary functions meet electromagnetic waves: opportunities and promises. *Adv Opt Mater* **8**, 2001194 (2020).
14. Krasikov S, Tranter A, Bogdanov A, Kivshar Y. Intelligent metaphotonics empowered by machine learning. *Opto-Electron Adv* **5**, 210147 (2022).
15. Zeng C, Lu H, Mao D, Du YQ, Hua H et al. Graphene-empowered dynamic metasurfaces and metadevices. *Opto-Electron Adv* **5**, 200098 (2022).
16. Luo XG. Metamaterials and metasurfaces. *Adv Opt Mater* **7**, 1900885 (2019).
17. Luo XG. Metasurface waves in digital optics. *J Phys Photonics* **2**, 041003 (2020).
18. Huang YJ, Luo J, Pu MB, Guo YH, Zhao ZY et al. Catenary electromagnetics for ultra-broadband lightweight absorbers and large-scale flat antennas. *Adv Sci* **6**, 1801691 (2019).
19. Yu P, Besteiro LV, Huang YJ, Wu J, Fu L et al. Broadband metamaterial absorbers. *Adv Opt Mater* **7**, 1800995 (2019).
20. Huang YJ, Xiao TX, Xie ZW, Zheng J, Su YR et al. Multistate nonvolatile metamirrors with tunable optical chirality. *ACS Appl Mater Interfaces* **13**, 45890–45897 (2021).
21. Cao T, Lian M, Chen XY, Mao LB, Liu K et al. Multi-cycle reconfigurable THz extraordinary optical transmission using chalcogenide metamaterials. *Opto-Electron Sci* **1**, 210010 (2022).
22. Song MW, Wang D, Peana S, Choudhury S, Nyga P et al. Colors with plasmonic nanostructures: a full-spectrum review. *Appl Phys Rev* **6**, 041308 (2019).
23. Song MW, Wang D, Kudyshev ZA, Xuan Y, Wang ZX et al. Enabling optical steganography, data storage, and encryption with plasmonic colors. *Laser Photonics Rev* **15**, 2000343 (2021).
24. Wang SM, Wu PC, Su VC, Lai YC, Chen MK et al. A broadband achromatic metalens in the visible. *Nat Nanotechnol* **13**, 227–232 (2018).
25. Chen WT, Zhu AY, Sanjeev V, Khorasaninejad M, Shi ZJ et al. A broadband achromatic metalens for focusing and imaging in the visible. *Nat Nanotechnol* **13**, 220–226 (2018).
26. Qin F, Liu BQ, Zhu LW, Lei J, Fang W et al. π-phase modulated monolayer supercritical lens. *Nat Commun* **12**, 32 (2021).
27. Wang YL, Fan QB, Xu T. Design of high efficiency achromatic metalens with large operation bandwidth using bilayer architecture. *Opto-Electron Adv* **4**, 200008 (2021).
28. Fan QB, Xu WZ, Hu XM, Zhu WQ, Yue T et al. Trilobite-inspired neural nanophotonic light-field camera with extreme depth-of-field. *Nat Commun* **13**, 2130 (2022).
29. Yang YH, Jing LQ, Zheng B, Hao R, Yin WY et al. Full-polarization 3D metasurface cloak with preserved amplitude and phase. *Adv Mater* **28**, 6866–6871 (2016).
30. Qian C, Zheng B, Shen YC, Jing L, Li EP et al. Deep-learning-enabled self-adaptive microwave cloak without human interven-

tion. *Nat Photonics* **14**, 383–390 (2020).
31. Yue Z, Li JT, Li J, Zheng CL, Liu JY et al. Terahertz metasurface zone plates with arbitrary polarizations to a fixed polarization conversion. *Opto-Electron Sci* **1**, 210014 (2022).
32. Chen Y, Yang XD, Gao J. 3D Janus plasmonic helical nanoapertures for polarization-encrypted data storage. *Light Sci Appl* **8**, 45 (2019).
33. Huo PC, Zhang S, Fan QB, Lu YQ, Xu T. Photonic spin-controlled generation and transformation of 3D optical polarization topologies enabled by all-dielectric metasurfaces. *Nanoscale* **11**, 10646–10654 (2019).
34. Han BW, Li SJ, Li ZY, Huang GS, Tian JH et al. Asymmetric transmission for dual-circularly and linearly polarized waves based on a chiral metasurface. *Opt Express* **29**, 19643–19654 (2021).
35. Li ZY, Li SJ, Han BW, Huang GS, Guo ZX et al. Quad-band transmissive metasurface with linear to dual-circular polarization conversion simultaneously. *Adv Theory Simul* **4**, 2100117 (2021).
36. Li SJ, Li ZY, Han BW, Huang GS, Liu XB et al. Multifunctional coding metasurface with left and right circularly polarized and multiple beams. *Front Mater* **9**, 854062 (2022).
37. Li X, Chen LW, Li Y, Zhang XH, Pu MB et al. Multicolor 3D meta-holography by broadband plasmonic modulation. *Sci Adv* **2**, e1601102 (2016).
38. Zhang XH, Pu MB, Guo YH, Jin JJ, Li X et al. Colorful metahologram with independently controlled images in transmission and reflection spaces. *Adv Funct Mater* **29**, 1809145 (2019).
39. Huang YJ, Xiao TX, Xie ZW, Zheng J, Su YR et al. Single-layered reflective metasurface achieving simultaneous spin-selective perfect absorption and efficient wavefront manipulation. *Adv Opt Mater* **9**, 2001663 (2021).
40. Gao H, Fan XH, Xiong W, Hong MH. Recent advances in optical dynamic meta-holography. *Opto-Electron Adv* **4**, 210030 (2021).
41. Meymand RE, Soleymani A, Granpayeh N. All-optical AND, OR, and XOR logic gates based on coherent perfect absorption in graphene-based metasurface at terahertz region. *Opt Commun* **458**, 124772 (2020).
42. Zhang ZJ, Yang JB, Bai W, Han YX, He X et al. All-optical switch and logic gates based on hybrid silicon-$Ge_2Sb_2Te_5$ metasurfaces. *Appl Opt* **58**, 7392–7396 (2019).
43. Zhao ZH, Wang Y, Ding XM, Li HY, Fu JH et al. Compact logic operator utilizing a single-layer metasurface. *Photonics Res* **10**, 316–322 (2022).
44. Gazzano O, Almeida MP, Nowak AK, Portalupi SL, Lemaître A et al. Entangling quantum-logic gate operated with an ultrabright semiconductor single-photon source. *Phys Rev Lett* **110**, 250501 (2013).
45. Schmidt-Kaler F, Häffner H, Riebe M, Gulde S, Lancaster GPT et al. Realization of the Cirac–Zoller controlled-NOT quantum gate. *Nature* **422**, 408–411 (2003).
46. Bliokh KY, Rodríguez-Fortuño FJ, Nori F, Zayats AV. Spin–orbit interactions of light. *Nat Photonics* **9**, 796–808 (2015).
47. Mueller JPB, Rubin NA, Devlin RC, Groever B, Capasso F. Metasurface polarization optics: independent phase control of arbitrary orthogonal states of polarization. *Phys Rev Lett* **118**, 113901 (2017).
48. Huo PC, Zhang C, Zhu WQ, Liu MZ, Zhang S et al. Photonic spin-multiplexing metasurface for switchable spiral phase contrast imaging. *Nano Lett* **20**, 2791–2798 (2020).
49. Zhang F, Pu MB, Li X, Gao P, Ma XL et al. All-dielectric metasurfaces for simultaneous giant circular asymmetric transmission and wavefront shaping based on asymmetric photonic spin–orbit interactions. *Adv Funct Mater* **27**, 1704295 (2017).
50. Mansuripur M. *Classical Optics and Its Applications* (Cambridge University Press, Cambridge, 2002).
51. Pu MB, Li X, Ma XL, Wang YQ, Zhao ZY et al. Catenary optics for achromatic generation of perfect optical angular momentum. *Sci Adv* **1**, e1500396 (2015).
52. Chen K, Ding GW, Hu GW, Jin ZW, Zhao JM et al. Directional janus metasurface. *Adv Mater* **32**, 1906352 (2020).
53. Sun QR, Zhang ZJ, Huang YJ, Ma XL, Pu MB et al. Asymmetric transmission and wavefront manipulation toward dual-frequency meta-holograms. *ACS Photonics* **6**, 1541–1546 (2019).
54. Georgi P, Wei QS, Sain B, Schlickriede C, Wang YT et al. Optical secret sharing with cascaded metasurface holography. *Sci Adv* **7**, eabf9718 (2021).
55. Zhang XH, Li X, Jin JJ, Pu MB, Ma XL et al. Polarization-independent broadband meta-holograms *via* polarization-dependent nanoholes. *Nanoscale* **10**, 9304–9310 (2018).
56. Huang LL, Mühlenbernd H, Li XW, Song X, Bai BF et al. Broadband hybrid holographic multiplexing with geometric metasurfaces. *Adv Mater* **27**, 6444–6449 (2015).
57. Groever B, Chen WT, Capasso F. Meta-lens doublet in the visible region. *Nano Lett* **17**, 4902–4907 (2017).
58. Arbabi A, Arbabi E, Kamali SM, Horie Y, Han S et al. Miniature optical planar camera based on a wide-angle metasurface doublet corrected for monochromatic aberrations. *Nat Commun* **7**, 13682 (2016).
59. Yu LG, Fan YB, Wang YJ, Zhang C, Yang WH et al. Spin angular momentum controlled multifunctional all-dielectric metasurface doublet. *Laser Photonics Rev* **14**, 1900324 (2020).

Acknowledgements

This work is supported by the National Natural Science Foundation of China (12104326, 12104329 and 62105228), Natural Science Foundation of Sichuan Province (2022NSFSC2000) and the Opening Foundation of State Key Laboratory of Optical Technologies on Nano-Fabrication and Micro-Engineering. P. Müller-Buschbaum acknowledges funding by Deutsche Forschungsgemeinschaft (DFG, German Research Foundation) under Germany´s Excellence Strategy – EXC 2089/1 – 390776260 (e-conversion) and TUM.solar in the context of the Bavarian Collaborative Research Project Solar Technologies Go Hybrid (SolTech). T. Xiao is grateful for the support from the China Scholarship Council (CSC).

Author contributions

Y. Huang and T. Xiao proposed the original idea. L. Li and P. Müller-Buschbaum supervised the project. Z. Xie, J. Zheng and J. Zhu participated the discussion of the research. S. Chen, Y. Su and W. Chen carried out the experiments and collected the data. Y. Huang, K. Liu and M. Tang analyzed all data. Y. Huang and L. Li wrote the paper. All authors discussed the results and commented on the manuscript

Competing interests

The authors declare no competing financial interests.

Supplementary information

Supplementary information for this paper is available at https://doi.org/10.29026/oea.2023.220073